Facilitating Large-Amplitude Motions of Wave Energy Converters in OpenFOAM by a Modified Mesh Morphing Approach

Johannes Palm and Claes Eskilsson

Abstract—**High-fidelity simulations using computational fluid dynamics (CFD) for wave-body interaction are becoming increasingly common and important for wave energy converter (WEC) design. The open source finite volume toolbox OpenFOAM® is one of the most frequently used platforms for wave energy. There are currently two ways to account for moving bodies in OpenFOAM: (i) mesh morphing, where the mesh deforms around the body; and (ii) an overset mesh method where a separate body mesh moves on top of a background mesh. Mesh morphing is computationally efficient but may introduce highly deformed cells for combinations of large translational and rotational motions. The overset method allows for arbitrarily large body motions and retains the quality of the mesh. However, it comes with a substantial increase in computational cost and possible loss of energy conservation due to the interpolation. In this paper we present a straightforward extension of the spherical linear interpolation (SLERP) based mesh morphing algorithm that increase the stability range of the method. The mesh deformation is allowed to be interpolated independently for different modes of motion, which facilitates tailored mesh motion simulations. The paper details the implementation of the method and evaluates its performance with computational examples of a cylinder with a moonpool. The examples show that the modified mesh morphing approach handles large motions well and provides a cost effective alternative to overset mesh for survival conditions.**

Index Terms—**wave energy converter, CFD, wave-body interaction, survival, extreme waves, OpenFOAM.**

I. Introduction

NUMERICAL models of wave energy converters (WECs) are of varying fidelity and come at different levels of computational cost [1]. The commonly used tool for basic design of WECs is the so-called wave-to-wire models (W2W), which are based on linear potential flow theory and accommodate time-domain simulations using radiation-diffraction theory or a pure Morison formulation for the hydrodynamic forces and responses of the WEC. They have been applied to a multitude of WECs, see e.g [2]–[4]. However, there are many situations where the WEC response is outside the range of validity of W2W models. Examples include severe storm waves with large wave height and a high steepness (typical survival situations), green water effects, breaking waves and large amplitude motion response. For these situations, WEC developers typically resort to physical model tests and/or computational fluid dynamics (CFD) simulations [5] for reliable predictions of the device response.

The most commonly used CFD model for WECs solves the Reynolds averaged Navier-Stokes equations with the volume of fluid method (VOF-RANS) for capturing the air-water interface (the free surface). The amount of studies applying VOF-RANS for WEC applications have steadily increased over the last decade, see e.g. [6], [7]. Using CFD as a design tool for WECs has its challenges, as a complete model needs to handle: (i) wave generation and absorption [8], [9]; (ii) extreme wave loads [10]; (iii) non-linear control [11], [12]; (iv) mooring dynamics [13], [14]; and (v) scale effects [15], [16].

Solving the VOF-RANS equations using the finite volume method requires a computational mesh, which entails a choice of how to treat the mesh when the WEC is moving in the waves. There are several ways to account for rigid body motion in VOF-RANS simulations. Different methods require different designs of the mesh layout, with refinement regions that match expected areas of interest etc. An ideal method should be computationally efficient, accurate and robust to arbitrarily large motions of the body.

A. Handling of moving rigid bodies in CFD

Different numerical platforms have different approaches to rigid body motion. One example is the immersed boundary method [17], implemented e.g. in Flow3D [18]. Here the rigid body is converted to an equivalent pressure surface applied in the equation of motion. As such it allows for arbitrarily large motions of the body, but the background mesh needs to be refined accordingly.

However, the most frequent way to deal with moving bodies is to use an arbitrary Lagrangian-Eulerian (ALE) approach [19]. In this method, the grid points can be moved with the flow (Lagrangian formulation), held fixed (Eulerian formulation), or moved in some

---

Paper submitted on 17 Dec. 2021; published 19 December 2022.

This work was supported by the Swedish Energy Agency under project numbers 40428-1 and 47264-1.

J. Palm is with Sigma Energy and Marine AB, Ekelundsgatan 1, Gothenburg, Sweden (e-mail: johannes.palm@sigma.se).

C. Eskilsson is with the Renewable Energy Unit, RISE – Research Institutes of Sweden, Box 857, SE-501 15 Borås, Sweden (e-mail: claes.eskilsson@ri.se); and the Department of the Built Environment, Aalborg University, Thomas Manns Vej 23, DK-9220 Aalborg Ø, Denmark (e-mail: claese@build.aau.dk).

Digital Object Identifier: https://doi.org/10.36688/imej.5.257-264

user defined (arbitrary) way to smoothen the transition zone between the Eulerian and Lagrangian parts. A key step in the ALE method is the mesh update. We highlight a few of the many available mesh update methods:

- re-meshing. For very large motions the mesh may have to be re-generated. This involves changing the mesh topology. It is therefore a costly and involved option;
- overset mesh. The solution is interpolated between a moving body domain (the overset mesh) and a static background domain.
- deforming mesh. Move the grid-points at the body boundary, and then solve for the remaining grid point motion using e.g. Laplacian diffusion [20], spherical linear interpolation (SLERP) [21], radial basis functions (RBF) [22], etc.

The overset mesh (OSM) method (implemented in e.g. STAR-CCM+ [23] and OpenFOAM [24]) is in theory providing a framework for arbitrary rigid body motion within the computational domain. The fluid properties are interpolated between a dynamic body mesh and a static background mesh. The fluid state information is at each time interpolated between the body mesh and the background mesh. The interpolation has to identify overlapping cells and compute relevant interpolation weights. Hence, the exchange of information takes place near the edges of the body mesh (often referred to as fringe cells). There are also cases where the interpolation causes loss of conservation of mass [25], however, several authors have found a good match between OSM method CFD simulations and physical wave tank tests [26]. As mentioned above, in the OSM the body mesh moves independently across the background mesh. In cases with a uniform background mesh, the motion amplitude can indeed be arbitrarily large. However for surface-piercing WEC applications there is a complication that is seldom pointed out. The fringe cell size should match the resolution of the free-surface, which is typically refined by a wave-band of higher resolution in the background mesh. For a high-quality simulation, the background mesh therefore needs a body-region of increased resolution to the level of the fringe cells. As such, it is highly beneficial to both quality and computational time to have a-priori estimates of the body motion.

For wave-energy applications, the most commonly used method amongst the deforming mesh approaches is the mesh morphing method (MM). The grid deforms (morphs) in a region surrounding the body motion so that the body motion can be taken into account. The method is very efficient (particularly when deformation is computed from pre-computed motion scales), and it is fair to say that for cases where it is suitable, the MM is always to prefer to the OSM on the account of a significant difference in computational speed. However its performance is sensitive to the mesh design of the numerical wave tank and the size of the deforming region, which the motion amplitude may not exceed. It is also bound to the initial topology of the mesh, so it only accommodates moderate motion amplitudes of the WEC. Indeed, in a recent comparison between the MM and the OSM methods of OpenFOAM, Windt et al. [27] labels the MM unsuitable for many large-amplitude cases without a-priori knowledge of the motion response.

B. *Paper contribution*

We present a modification to the SLERP based mesh morphing method in OpenFOAM. The modification yields a method that is less sensitive to the mesh design and can be tailored to accommodate very large surge and sway offsets without affecting the overall mesh quality. The modification comes with virtually no extra computational cost, but increases both stability, quality and flexibility of CFD simulations for floating WECs. We will thus compare three mesh motion techniques using OpenFOAM: (i) the original mesh morphing (MMO) algorithm; (ii) the overset mesh (OSM) method; and (iii) the suggested modified morphing method (MMM). The modified mesh morphing method is exemplified on the cylinder with a moonpool used in CCP-WSI blind test 3 case [28].

II. GOVERNING EQUATIONS

The incompressible Reynolds Averaged Navier-Stokes (RANS) equations for a fluid mixture in an ALE formulation read:

$$\nabla \cdot \vec{u}_{\mathrm{r}} = 0\,, \tag{1}$$

$$\frac{\partial}{\partial t}\left(\rho\,\vec{u}\right) + \nabla \cdot \left(\rho \vec{u} \vec{u}_{\mathrm{r}}\right) = -\nabla p + \nabla \cdot \mathbf{S} + \rho\,\vec{f_b}\,, \tag{2}$$

with the following notation: $\vec{u}$ - fluid velocity; $\vec{u}_{\mathrm{r}} = \vec{u} - \vec{u}_{\mathrm{g}}$ - fluid velocity relative to the grid velocity $\vec{u}_{\mathrm{g}}$; p - pressure; ρ - mixture density; $\mathbf{S}$ - the viscous stress tensor; and $\vec{f_b}$ - the body force. OpenFOAM solves the NS equations with a cell-centred 2nd order finite volume method on unstructured polyhedral cells.

We use the volume of fluid (VOF) method and approximate the two-phase air-water problem as a single phase mixture with a phase fraction $\alpha \in [0, 1]$, which indicates air or water for $\alpha = 0$ and $\alpha = 1$ respectively. The phase fraction α is subject to the transport equation

$$\frac{\partial \alpha}{\partial t} + \nabla \cdot \left(\alpha \vec{u}_{\mathrm{r}}\right) \;=\; 0\,. \tag{3}$$

Fluid properties such as density (ρ) and kinematic viscosity (ν) are linearly interpolated as

$$\rho \;=\; \alpha \rho_w + (1-\alpha)\,\rho_a\,, \tag{4}$$

$$\nu \;=\; \alpha \nu_w + (1-\alpha)\,\nu_a\,, \tag{5}$$

where the indices w and a denote water and air, respectively.

The grid velocity $\vec{u}_{\mathrm{g}}$ can be computed from the mesh displacement due to the motion of a moving rigid body.

The motion of a rigid floating body is governed by Newton's II law:

$$m_b \frac{\partial^2 \hat{\eta}}{\partial t^2} = \int_K \left(\sigma - \mathbf{n}p\right) \mathrm{d}K + F_{moor}\,, \tag{6}$$

$$I_b \frac{\partial^2 \hat{\Omega}}{\partial t^2} = \int_K r_{CK}\left(\sigma - \mathbf{n}p\right) \mathrm{d}K + M_{moor}\,, \tag{7}$$

in which m_b and I_b are the body mass and inertia; and $\hat{\eta}$ and $\hat{\Omega}$ are the translational and rotational degrees-of-freedom. The pressure p and shear σ acts on the body surface K with the outward normal $\mathbf{n}$ and position vector r_{CK} relative to the centre of gravity. F_{moor} is the mooring force and the corresponding moment M_{moor}.

III. THE EXISTING MESH MORPHING METHOD

The starting point of our analysis is the native mesh morphing capability of the rigid body solver in OpenFOAM. The body state is described by its position $\vec{B}(t)$ and its orientation $\mathbf{q}(t)$. The position is the sum of the initial position $\vec{B}_0$ and the body displacement $\vec{b}(t)$. The orientation $\mathbf{q}(t)$ is expressed in quaternion notation indicated by bold font, and we denote the initial orientation of the body as $\mathbf{q}_0$. The point displacement $\vec{\delta p}_i$ of a point $\vec{P}_i$ (relative to the initial body position in the initial mesh) can then be computed as

$$\vec{\delta p}_i = \beta_i \vec{b} + \mathbf{q}_{\beta_i}\mathbf{P}_i\mathbf{q}^*_{\beta_i}\,, \tag{8}$$

$$\beta_i = \begin{cases} 1 & \text{if} \quad W(\vec{P}_i) < r_{\text{in}} \\ 0 & \text{if} \quad W(\vec{P}_i) > r_{\text{out}} \\ 1 - \dfrac{W(\vec{P}_i) - r_{\text{in}}}{r_{\text{out}} - r_{\text{in}}} & \text{otherwise} \end{cases}\,, \tag{9}$$

$$\mathbf{q}_{\beta_i} = \left(\mathbf{q}\mathbf{q}_0^{-1}\right)^{\beta_i}\mathbf{q}_0\,, \tag{10}$$

where β_i is the interpolation weight of point i, * symbolises quaternion conjugate, and $W(\vec{P}_i)$ is the minimum distance from the point to the surface of the body. In (9), r_{in} defines an inner region where the point motion follows the body rigidly. In the same way, the mesh is static for $W(\vec{P}_i) > r_{\text{out}}$ (see Fig. 1). The original mesh morphing method is labelled MMO throughout the paper.

IV. A MODIFIED MESH MORPHING METHOD

The rotational motion is particularly challenging for WEC applications. Maintaining a good quality mesh during large roll or pitch amplitudes of a point-absorbing device requires a significant cell count around the body so that the air-water interface is well resolved at all times. For a good quality simulation, we would like the upstream and downstream mesh in the nearfield to be equally distorted by rotational motion. The MMO method can only achieve this without surge motion. If we apply a wave-drift force or drag from an ocean current, the MMO method compresses the downstream mesh, and coarsens the upstream mesh within the rotational region causing also the mesh quality to differ between the two sides.

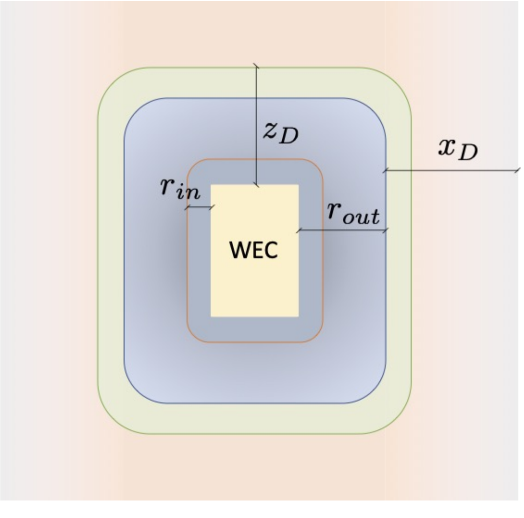

Fig. 1. Illustration of variables used to define the mesh morphing.

The idea is simple. We extend the MMO method by allowing three additional morphing scales, one for each translational degree of freedom. The surge (x), sway (y) and heave (z) motions of the body are thus morphed independently according to the scales $\alpha^{(x)}$, $\alpha^{(y)}$ and $\alpha^{(z)}$, respectively. Equation (8) is then modified as

$$\vec{\delta p}_i = [\alpha_i^{(x)} b_x, \alpha_i^{(y)} b_y, \alpha_i^{(z)} b_z] + \mathbf{q}_{\beta_i}\mathbf{P}_i\mathbf{q}^*_{\beta_i}\,, \tag{11}$$

with the scales defined as

$$\alpha_i^{(x)} = \begin{cases} 1 - \min\left(\dfrac{x_i - R_x^+}{x_{\text{D}}}, 1\right) & \text{if} \quad x_i > R_x^+ \\ 1 - \min\left(\dfrac{R_x^- - x_i}{x_{\text{D}}}, 1\right) & \text{if} \quad x_i < R_x^- \\ 1 & \text{otherwise} \end{cases}\,, \tag{12}$$

$$\alpha_i^{(z)} = 1 - \max\left(0, \min\left(1, \frac{W(\vec{P}_i) - r_{\text{in}}}{z_{\text{D}} - r_{\text{in}}}\right)\right)\,. \tag{13}$$

The $\alpha_i^{(y)}$ scale is computed analogously with $\alpha_i^{(x)}$ in (12). The points $\vec{R}^+$ and $\vec{R}^-$ define the bounding box (top right and bottom left corner respectively) of all points with rotation scale $\beta_i > 0$. Hence, the morphing rotation region will translate as a rigid body horizontally, and its deformation will be interpolated over a distance x_D and y_D respectively. The mesh displacement from heave will be independently interpolated between distances r_{in} and z_D and added to the total point displacement (see Fig. 1). The implementation is limited to box-shaped domains, as the mesh points are calculated to slide along the outer faces of the domain. This also makes the model suitable for shallow water applications where the water depth limits the deformation zone size in the MMO method. The modified mesh morphing method is labelled MMM throughout the paper.

V. NUMERICAL TEST CASE

We here use the CCP-WSI test case 3 of a cylinder with a moonpool moored with a single point-mooring in the form of a pre-tensioned linear spring [28]. See Table I for the buoy and mooring details. The experiments of the body response to focused wave impacts [29] were conducted at the University of Plymouth, however, here we study equivalent regular maximum waves of the same sea-state.

A. *Numerical wave tank*

The computational domain is (W_X, W_Y, W_Z)=(29.6, 15.6, 6) m, with global coordinate system origin in the centre of the domain. The still water level (SWL) is at $z = 0$, the water depth is 3 m, and the buoy is

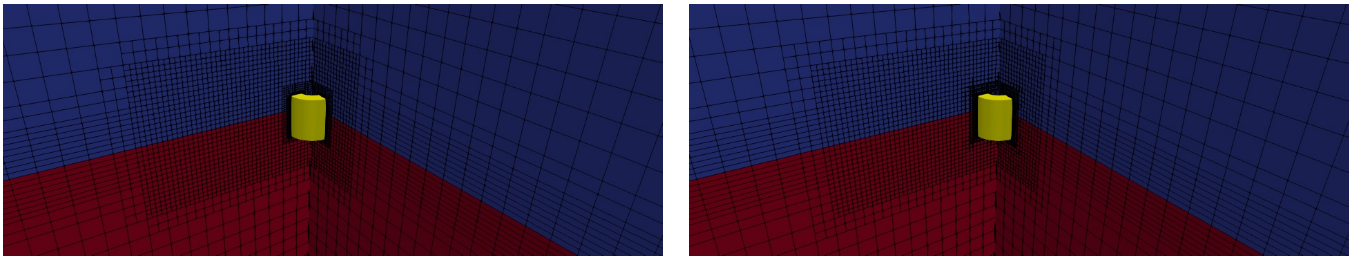

(a) Zoom around the body - MMM and MMO

(b) Zoom around the body - OSM

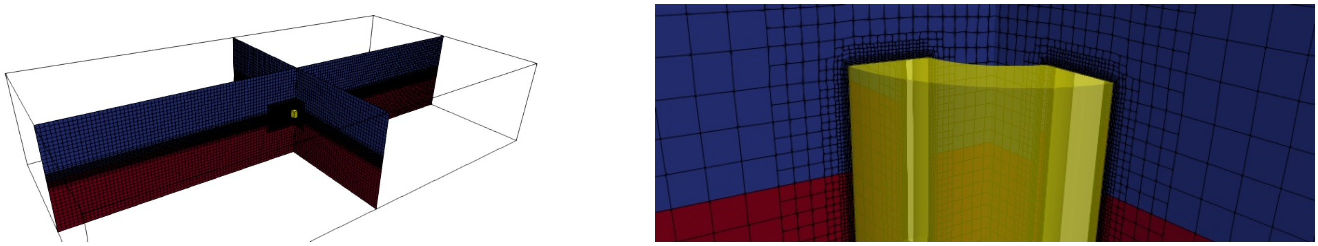

(c) Global mesh layout

(d) Zoom showing the boundary layers

Fig. 2. Computational mesh for the CCP-WSI test case 3, illustrating the overall mesh layout,the boundary layer and the similarity between the mesh morphing and the overset meshes.

TABLE I
PROPERTIES OF THE MOONPOOL BUOY AND ITS MOORING SPRING. VERTICAL POSITIONS z ARE IN THE GLOBAL COORDINATE SYSTEM WITH ORIGIN AT THE STILL WATER LEVEL.

Label	**Value**	**Property**
M (kg)	61.459	Buoy mass
$I_\perp$ (kgm^2)	3.56	Moment of inertia (roll and pitch).
I_z (kgm^2)	3.298	Yaw moment of inertia.
D (m)	0.577	Outer hull diameter
D_mp (m)	0.289	Moonpool diameter
H (m)	0.500	Total height
z_g^* (m)	0.152	Centre of gravity from buoy bottom.
Z_g (m)	-0.178	Centre of gravity in global coordinates.
Z_m (m)	-0.33	Moored draft (mooring point)
K (N/m)	67	Mooring spring stiffness
L_0 (m)	2.	Rest length of mooring spring
F_eq (N)	31.55	Mooring pretension at rest

initially placed at (X, Y, Z) = (0, 0, Z_g). The aim of our current investigation is to compare the performance of different mesh motion models. For a good comparison of model performance we only require a *representative* body motion, rather than one which is perfectly *accurate*. We therefore use a coarse model setup for our test suite to save computational expense. Fig. 2 shows the layout of the computational grids used in the simulation campaign. The two grids, one for the MM simulations and one for the OSM simulations, were designed to be as equivalent in size as possible, differing only by necessity around the buoy hull (compare Figs. 2a and 2b). The MMM and MMO mesh had 905 000 cells and the OSM mesh had a total of 914 000 cells. The body mesh employed two levels of local cell refinement surrounding the WEC hull, as well as a boundary layer of 5 cells with expansion ratio 1.1, see the details in Fig. 2d.

TABLE II
PROPERTIES OF THE MESH MORPHING METHODS USED IN THE SIMULATIONS. SEE FIG. 1.

Method	r_i	r_o	x_D	y_D	z_D	Ξ
MMO	0.1	1.0	-	-	1.0	1.0
MMM–332	0.1	1.0	3.0	3.0	2.0	4.0
MMM -112	0.1	1.0	1.0	1.0	2.0	2.0

For comparison we introduce the X-range Ξ of the deforming mesh region as the distance from the bounding box of the WEC hull to the edge of the dynamic mesh region. For the MMO method $\Xi = r_\mathrm{o}$, whereas for the MMM method $\Xi = r_\mathrm{o} + x_D$, see (12). Table II describe the properties of the mesh morphing methods used in the paper.

Table II details the numerical settings used in the simulation. The mesh deformation parameters, in particular the outer diameter, were knowingly selected to explore a case with high deformation in the MMO method. Two settings of MMM were used to illustrate its performance.

VI. VERIFICATION OF IMPROVEMENTS

We illustrate the benefits of the modified mesh-morphing approach by viewing how the cell-quality changes with the horizontal displacement of a rotated body. The buoy described in Table I is first rotated -30 deg in pitch, and is then displaced in the XZ-plane by a distance $(\delta X, \delta Z)$. We present results for $\delta X \in [0, 1.2]$ m, and $\delta Z = 0$, and 0.2 m. The rotational region was specified with $r_\mathrm{o} = 1$ m. In addition, the modified morphing method uses a 3 m region in x and a 2 m region in z over which the mesh is smoothed.

The resulting mesh motion can be seen in Fig. 3, with corresponding mesh quality data shown in Table III. As expected, the original morphing algorithm fails to accommodate the very large horizontal displacement.

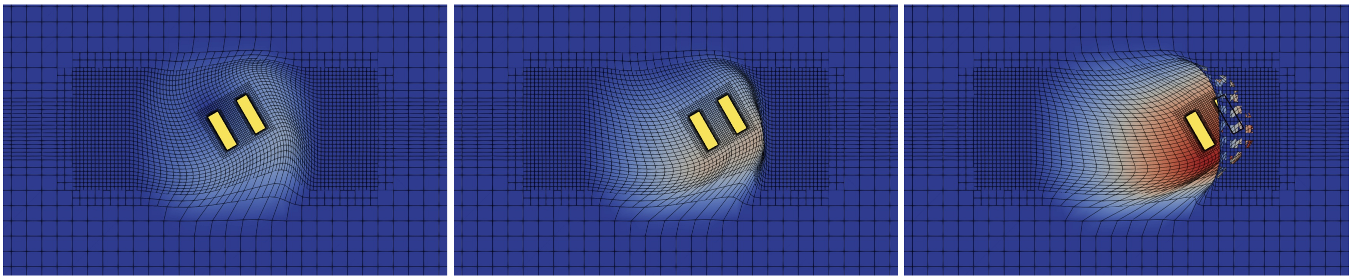

(a) MMO, $(\delta X, \delta Z) = (0.2, 0.0)$ m (b) MMO, $(\delta X, \delta Z) = (0.6, 0.0)$ m (c) MMO, $(\delta X, \delta Z) = (1.2, 0.0)$ m

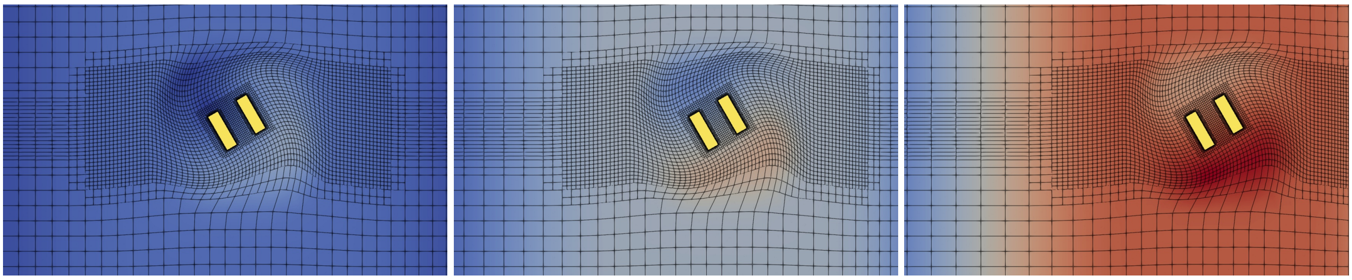

(d) MMM, $(\delta X, \delta Z) = (0.2, 0.0)$ m (e) MMM, $(\delta X, \delta Z) = (0.6, 0.0)$ m (f) MMM, $(\delta X, \delta Z) = (1.2, 0.0)$ m

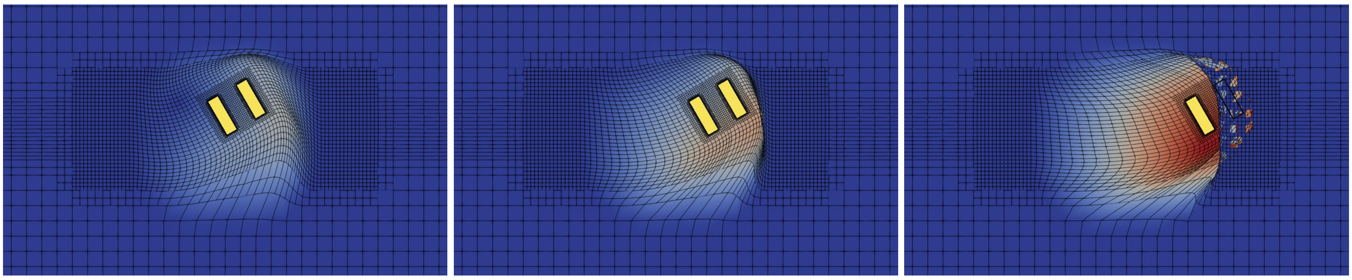

(g) MMO, $(\delta X, \delta Z) = (0.2, 0.2)$ m (h) MMO, $(\delta X, \delta Z) = (0.6, 0.2)$ m (i) MMO, $(\delta X, \delta Z) = (1.2, 0.2)$ m

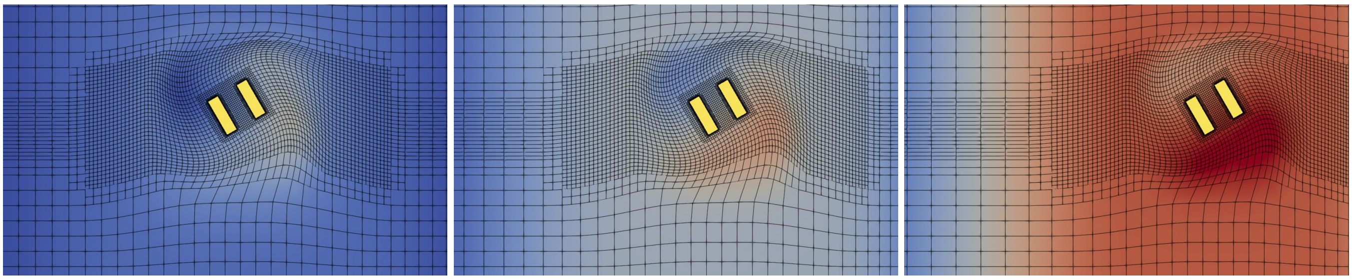

(j) MMM, $(\delta X, \delta Z) = (0.2, 0.2)$ m (k) MMM, $(\delta X, \delta Z) = (0.6, 0.2)$ m (l) MMM, $(\delta X, \delta Z) = (1.2, 0.2)$ m

Fig. 3. Illustrative difference between the MMO and MMM methods for rigid body horizontal (X) and vertical (Z) displacements. A -30 deg pitch rotation is applied to all figures. The color scale from blue(min) to red(max) represent point-displacement magnitude.

TABLE III
Mesh quality values of max. aspect ratio (A.R.), max. non-orthogonality (N.O.) and max. skewness for the MMO and MMM methods. The buoy is rotated 30 deg and is displaced by $(\delta X, \delta Z)$ m in the (X, Z) plane. IM indicates an illegal mesh.

	$\delta Z = 0$								$\delta Z = 0.2$							
	$\delta X = 0.2$		$\delta X = 0.4$		$\delta X = 0.6$		$\delta X = 1.2$		$\delta X = 0.2$		$\delta X = 0.4$		$\delta X = 0.6$		$\delta X = 1.2$	
Property	**MMO**	**MMM**	**MMO**	**MMM**	**MMO**	**MMM**	**MMO**	**MMM**	**MMO**	**MMM**	**MMO**	**MMM**	**MMO**	**MMM**	**MMO**	**MMM**
A.R.	4.78	4.78	9.20	4.96	IM	5.39	IM	6.67	8.5	4.78	14.7	4.96	IM	5.39	IM	6.67
Non-Ortho	64.7	64.6	82.1	64.6	IM	64.6	IM	64.6	78.8	69.0	88.7	69.0	IM	69.0	IM	69.0
Skewness	3.24	3.24	3.24	3.24	IM	3.24	IM	3.24	3.24	3.24	3.24	3.24	IM	3.24	IM	3.24

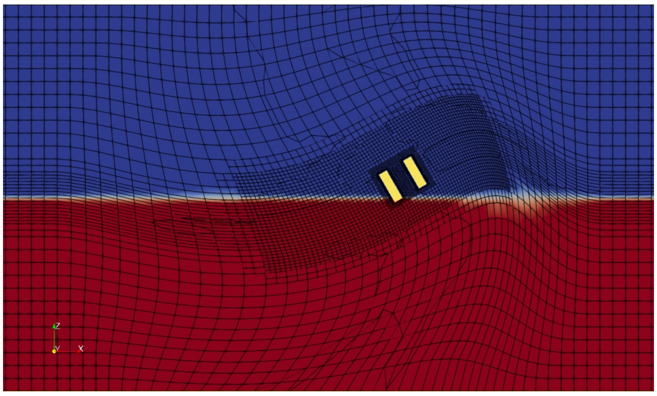

Fig. 4. Mesh motion results of the largest displacement $(\delta X, \delta Z) = (1.2, 0.2)$ m for the MMO method with $r_o = 4$ m. The figure shows fluid phase fraction (red is water, blue is air).

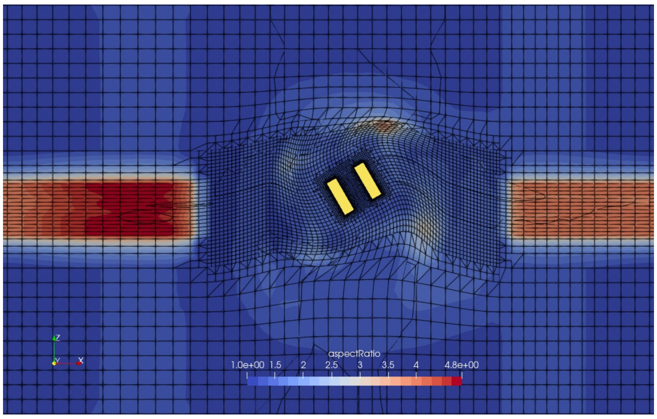

Fig. 5. Aspect ratio during mesh motion of the MMM method with $\Xi = x_D + r_o = 4$ m at the largest displacement $(\delta X, \delta Z) = (1.2, 0.2)$ m.

Indeed, it fails already before $\delta X = 0.6 r_{\text{out}}$ (r_{out}=1 m). The decoupled approach implemented in the modified method efficiently avoids this problem and maintains an acceptable quality mesh also during large amplitude motion.

The X-range of the morphing region is $\Xi = x_D + r_{\text{out}}$ for the MMM method. Now, of course the external region of deformation is significantly larger for the MMM algorithm than for the OM method (4 to 1), and herein lies part of the explanation to the large improvements shown in Table III and Fig. 3. However, the MMO method lacks the flexibility to generate such a large domain. In Fig. 4, we illustrate how an equivalent MMO method simulation with the same morphing domain extension ($\Xi = r_{\text{out}} = 4$ m) as the MMM method would have looked. This simple test highlights two well-known issues with the MMO method: (i) that the domain size would have to be increased vertically to accommodate for such a large morphing domain ($Z \in \pm 3$ m), which would be possible but costly for cases with larger water depth; and (ii) that the wave band of cell refinement that surrounds the free surface has to be increased to avoid coarser cells to cross the free surface. In contrast, Fig. 5 shows how the MMM aspect ratio increases to its maximum to the left of the buoy, inside the waveband where the cells have AR=4 in the initial mesh. The increase in AR may result in excessive wave damping in the incoming wave field, however, there is no reason not to use a significantly larger x_D region in the MMM method. This would decrease the relative mesh distortion and maintain a better AR throughout the simulation. Please note that not only do the modified method maintain the wave region within its boundaries for all displacements in this test, but it also ensures that the maximum non-orthogonality of the cells is unaffected by the significant X-displacement of the WEC, see Table III.

VII. RESPONSE IN LARGE WAVES

A benchmark simulation in large waves was made to compare the results from three different methods for dynamic mesh handling. We use an equivalent regular maximum wave for the H_s =0.276 m, T_p =2.3 s sea-state described in [28]. The maximum regular wave is simply estimated as [30]: $H_{max} = 1.9\, H_s$=0.5206 m, $T = 0.92\, T_p$ =2.3 s, and is applied with waves propagating along the positive X-axis to the NWT described in Section V-A.

Both the OSM and the MMO methods have successfully been applied to this particular geometry in [28]. However, here we knowingly choose a very tight mesh morphing zone to stress test the stability range of the algorithms, as well as a coarse mesh overall. The following mesh motion simulations were investigated; OSM, MMO and two MMM with different settings for (x_D, y_D, z_D), see Table II. The first modified morphing simulation uses the above setting of 3 m in the horizontal directions and 2 m in the vertical (denoted MMM-332) and the second uses 1 m in the horizontal directions and 2 m in the vertical (denoted MMM-112).

Fig. 6 shows the motion of the buoy in surge, heave and pitch for the different methods. At 11.1 s the MMO simulation aborts due to mesh problems. The MMM-112 method fails soon after at 11.5 s. At the crash, the surge offset is 0.5 m, which correlates well with the failed mesh quality from the displacement tests for the MMO method (Table III), where 0.6 m showed a failed mesh for MMO. Up to the mesh failures the lines of the mesh morphing simulations are virtually on top of each other, and the results are quite similar. There is a slight difference in surge as the OSM shows a smaller surge offset. However, for the purpose of comparing mesh quality, stability of the simulations and computational time, the results are found to be sufficiently equal.

Fig. 7 illustrates the meshes at 11.1 s for the four simulations. The results exemplify several of the typical challenges for CFD design of WECs:

- Fig. 7a shows the illegal mesh compression and high-aspect ratio on the leeward side of the MMO method. Note that there is significant cell compression and skewness also above the WEC. The mesh was close to its limit also in the heave direction, and would have needed a larger r_{out} value.
- The MMM–112 mesh in Fig. 7b illustrates the effect of decoupling the DoFs. The cell quality is now good above the WEC, however the total x-motion is still on the limit of what the mesh can handle. Although compressed, the cell quality is

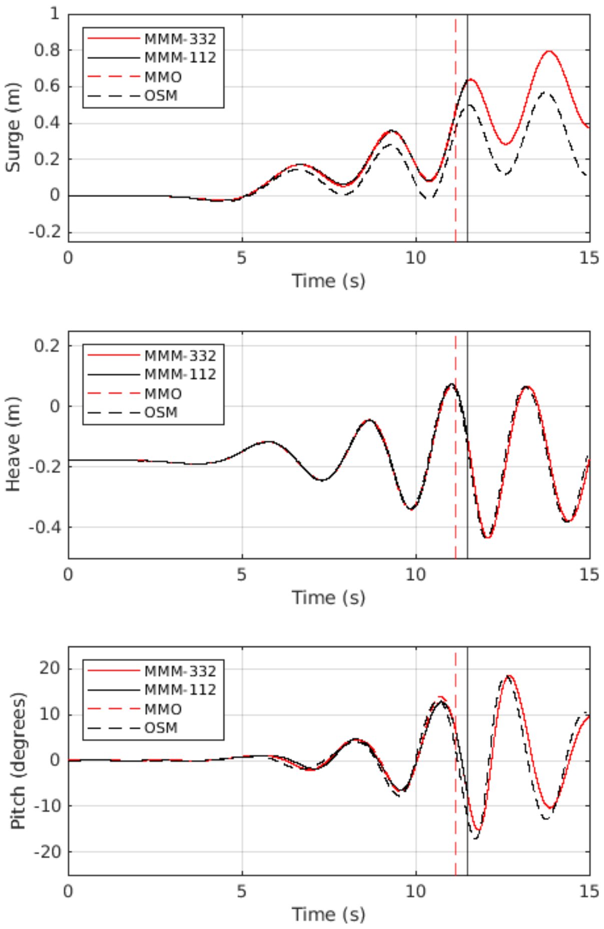

Fig. 6. Motion of the buoy in regular waves with $H = 9.52$ m and $T = 2.3$ s. The solid vertical lines indicates the time of mesh failures for the MMM-112 (black) and MMO (dashed red) mesh motion settings.

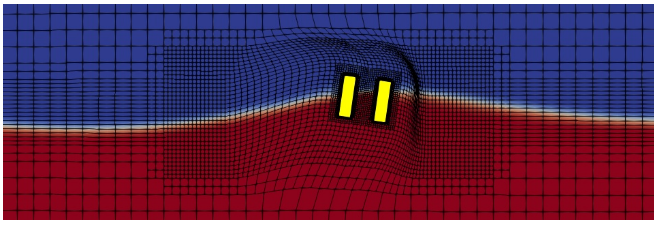
(a) MMO

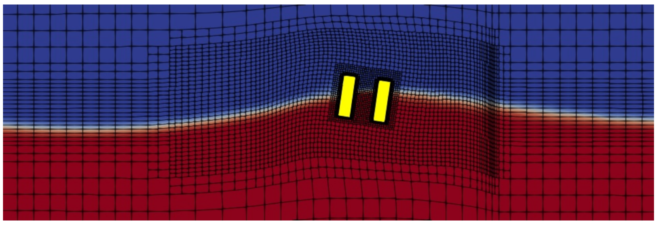
(b) MMM-112

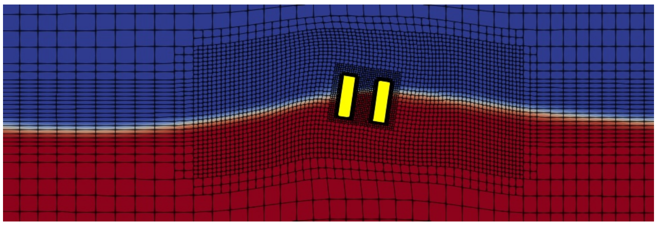
(c) MMM-332

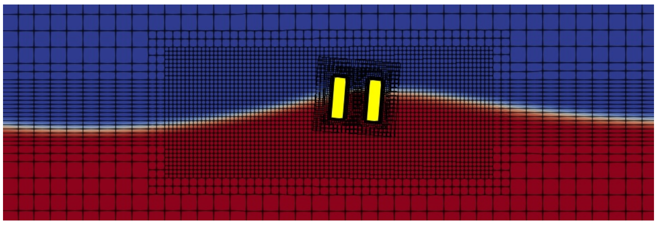
(d) OSM

Fig. 7. Computational mesh at time 11.1 s, right before the breakdown of the MMO method, for regular waves with $H = 9.52$ m and $T = 2.3$ s. The figures show fluid phase fraction (red is water, blue is air).

still good at $t = 11.1$ s as the cell deformation due to surge simply slides along the x-axis and does not introduce non-orthogonality or skewness. Only the aspect ratio and cell volume are affected.

- The MMM–332 shows how the MMM method can be used to handle large motions without significant mesh deformation. Fig. 7c displays a smooth cell displacement in all directions, and the cell quality is good overall by visual inspection.
- Although the overset mesh has no cell deformation and is overall of good quality, Fig. 7d shows how the body mesh has moved closer to the top of the refinement region of the background mesh. This is a clear example of the connection between the initial mesh design and a good estimate of the motion amplitude of the WEC.

Results from a benchmark simulation of computational time between the methods are presented in Table IV. We used 8 core parallel runs each for comparable results on a HP DL380 Gen 10 server (2 x Intel Xeon-Gold 5120, 2.2 GHz/14-core). The computational time is presented as seconds per core and wave period. As expected, the OSM (using the inverse distance interpolation method) is significantly more costly, whereas the two morphing methods are similar in performance. The MMM method performs slightly better, but the difference is judged to be small.

TABLE IV
COMPUTATIONAL TIMES OF THE THREE METHODS. TIME IS SHOWN AS SECONDS PER CPU AND WAVE PERIOD. THE SPEED-UP FACTOR REPRESENT THE SPEED RELATIVE TO THE OSM METHOD.

Method	**Time (s)**	**Speed-up (-)**
MMM	3412	1.80
MMO	3572	1.72
OSM	6139	1.00

VIII. CONCLUDING REMARKS

This paper exemplifies how a modified mesh motion algorithm can be implemented to increase the range of stability of a mesh morphing algorithm for wave-reacting bodies. The mesh displacement examples of Fig. 3 clearly illustrates the benefit of the modification in terms of maintaining a good quality mesh also for large amplitude motion of the device. We also show that a highly flexible domain can be achieved by individually choosing the interpolation range of each translational dof in the morphing method. Table IV shows that the extra computational time required by the modification is negligible (indeed, in this case it was even faster than the original). The original mesh morphing method is constrained to work in a single morphing domain with the same outer distance to all sides of the WEC, which may be limited in size by the height or depth of the NWT. The modified version uses an outer motion scale to handle surge motions, a region where the domain has to be large for purposes of wave propagation. Hence there are few spatial constraints, and the interpolation range x_D can often be chosen quite large, which obviously decreases the relative stretch of the mesh.

Finally, we highlight that the main benefit of using this modified approach is that it increases the allowable motion range of WECs. This has two effects: (i) that a larger class of WEC problems can be simulated with the computationally efficient mesh morphing approach, thus avoiding costly overset mesh simulations; and (ii) the demand of accurate a-priori estimates of body motion decreases as the mesh motion is more robust to large body displacements.

REFERENCES

[1] C. Eskilsson, J. Palm, A. Ensig-Karup, U. Bosi, and M. Ricchiuto, "Wave induced motions of point-absorbers: an hierarchical investigation of hydrodynamic models," in *Proc. 11th European Wave and Tidal Energy Conference*, Nantes, France, 2015.

[2] A. Babarit, J. Hals, M. Muliawan, A. Kurniawan, T. Moan, and J. Krokstad, "Numerical benchmarking study of a selection of wave energy converters," *Renewable Energy*, vol. 41, pp. 44–63, 2012.

[3] M. Penalba and J. Ringwood, "A review of wave-to-wire models for wave energy converters," *Energies*, vol. 9, no. 7, p. 506, Jun 2016. [Online]. Available: http://dx.doi.org/10.3390/en9070506

[4] M. Alves, *Wave-to-Wire Modelling of WECs*. Cham: Springer International Publishing, 2017, pp. 261–287. [Online]. Available: https://doi.org/10.1007/978-3-319-39889-1_10

[5] J.-W. Kim, H. Jang, A. Baquet, J. O'Sullivan, S. Lee, B. Kim, A. Read, and H. Jasak, "Technical and economical readiness review of CFD-based numerical wave tank for offshore floater design," in *Proceedings of Offshore Technology Conference*, Houston, USA, 2-5 May 2016, 2016.

[6] C. Eskilsson, J. Palm, J. Kofoed, and E. Friis-Madsen, "CFD study of the overtopping discharge rate of the Wave Dragon wave energy converter," in *Renewable Energies Offshore*, C. Guedes Soares, Ed. Taylor & Francis Group, November 2014, pp. 287–294.

[7] C. Windt, J. Davidson, and J. Ringwood, "High-fidelity numerical modelling of ocean wave energy systems: A review of computational fluid dynamics-based numerical wave tanks," *Renewable and Sustainable Energy Reviews*, vol. 93, pp. 610–630, 2018.

[8] P. Higuera, J. Lara, and I. Losada, "Realistic wave generation and active wave absorption for Navier-Stokes models application to OpenFOAM," *Coastal Engineering*, vol. 71, pp. 102–118, 2013.

[9] B. Paulsen, H. Bredmose, and H. Bingham, "An efficient domain decomposition strategy for wave loads on surface piercing circular cylinders," *Coastal Engineering*, vol. 86, pp. 57–76, 2014.

[10] E. J. Ransley, "Survivability of wave energy converter and mooring coupled system using cfd," Ph.D. dissertation, Plymouth University, 2015.

[11] G. Giorgi and J. Ringwood, "Implementation of latching control in a numerical wave tank with regular waves," *J. Ocean Eng. Mar. Energy*, vol. 2, pp. 211–226, 2016.

[12] W. Wang, M. Wu, J. Palm, and C. Eskilsson, "Estimation of numerical uncertainty in cfd simulations of a passively controlled wave energy converter," *Proc IMechE Part M: J Engineering for the Maritime Environment*, vol. 232, no. 1, pp. 71–84, 2018.

[13] J. Palm, C. Eskilsson, G. Paredes, and L. Bergdahl, "CFD simulations of a moored floating wave energy converter," in *Proc. 10th European Wave and Tidal Energy Conference*, Aalborg, Denmark, 2013.

[14] ——, "Coupled mooring analysis for floating wave energy converters using CFD: Formulation and validation," *Int. J. of Marine Energy*, vol. 16, pp. 83–99, 2016.

[15] H. Gu, P. Stansby, T. Stallard, and E. Carpintero Moreno, "Drag, added mass and radiation damping of oscillating vertical cylindrical bodies in heave and surge in still water," *J. Fluids Struct*, vol. 82, pp. 343–356, 2018.

[16] J. Palm, C. Eskilsson, L. Bergdahl, and R. Bensow, "Assessment of scale effects, viscous forces and induced drag on a point-absorbing wave energy converter by CFD simulations," *Journal of Marine Science and Engineering*, vol. 6, no. 4, p. 124, Oct 2018. [Online]. Available: http://dx.doi.org/10.3390/jmse6040124

[17] C. S. Peskin, "Flow patterns around heart valves: A numerical method," *Journal of Computational Physics*, vol. 10, no. 2, pp. 252–271, 1972. [Online]. Available: https://www.sciencedirect.com/science/article/pii/0021999172900654

[18] Flow3D, *Flow3D Homepage*, available http://www.flow3d.com.

[19] J. Donea, A. Huerta, J.-P. Ponthot, and A. Rodríguez-Ferran, *Arbitrary Lagrangian–Eulerian Methods*. John Wiley & Sons, Ltd, 2004, ch. 14. [Online]. Available: https://onlinelibrary.wiley.com/doi/abs/10.1002/0470091355.ecm009

[20] A. Winslow, "Equipotential zoning of two-dimensional meshes," University of California, Lawrence Livermore Laboratory, Livermore, CA, USA, Tech. Rep., 2005.

[21] K. Shoemake, "Animating rotation with quaternion curves," in *Special Interest Group on Computer Graphics and Interactive Techniques*, vol. 19, no. 3, San Francisco, USA, 1985.

[22] M. Biancolini, *Fast Radial Basis Functions for Engineering Application*. Springer, Cham, 2017.

[23] *Star-ccm+, User Guide*, CD-Adapco (Siemens), 2016.

[24] *OpenFOAM Homepage*, OpenCFD Ltd, 2018, available http://www.openfoam.org.

[25] D. D. Chandar, "On overset interpolation strategies and conservation on unstructured grids in openfoam," *Computer Physics Communications*, vol. 239, pp. 72–83, 2019. [Online]. Available: https://www.sciencedirect.com/science/article/pii/S0010465519300153

[26] H. Chen, L. Qian, Z. Ma, W. Bai, Y. Li, D. Causon, and C. Mingham, "Application of an overset mesh based numerical wave tank for modelling realistic free-surface hydrodynamic problems," *Ocean Engineering*, vol. 176, pp. 97–117, 2019. [Online]. Available: https://www.sciencedirect.com/science/article/pii/S0029801818317566

[27] C. Windt, J. Davidson, D. D. Chandar, N. Faedo, and J. V. Ringwood, "Evaluation of the overset grid method for control studies of wave energy converters in OpenFOAM numerical wave tanks," *Journal of Ocean Engineering and Marine Energy*, vol. 6, pp. 55–70, 2020.

[28] E. Ransley, S. Yan, S. Brown, M. Hann, D. Graham, C. Windt, P. Schmitt, J. Davidson, J. Ringwood, P.-H. Musiedlak, J. Wang, J. Wang, Q. Ma, Z. Xie, N. Zhang, X. Zheng, G. Giorgi, H. Chen, Z. Lin, L. Qian, Z. Ma, W. Bai, Q. Chen, J. Zang, H. Ding, L. Cheng, J. Zheng, H. Gu, X. Gong, Z. Liu, Y. Zhuang, D. Wan, H. Bingham, and D. Greaves, "A Blind Comparative Study of Focused Wave Interactions with Floating Structures (CCP-WSI Blind Test Series 3)," *International Journal of Offshore and Polar Engineering*, vol. 30, no. 01, pp. 1–10, 03 2020. [Online]. Available: https://doi.org/10.17736/ijope.2020.jc774

[29] M. Hann, D. Greaves, and A. Raby, "Snatch loading of a single taut moored floating wave energy converter due to focussed wave groups," *Ocean Engineering*, vol. 96, pp. 258–271, 2015.

[30] *NV-RP-C205: Envirnonmental Conditions and Environmental Loads.*, Det Norske Veritas, 2010.